# Origins of Extreme Liquid Repellency on Structured, Flat, and Lubricated Hydrophobic Surfaces

Dan Daniel,[1,2,*] Jaakko V. I. Timonen,[1,3] Ruoping Li,[4] Seneca J. Velling,[4] Michael J. Kreder,[1] Adam Tetreault,[4] and Joanna Aizenberg[1,4,5,†]

[1]John A. Paulson School of Engineering and Applied Sciences, Harvard University, Cambridge, Massachusetts 02138, USA
[2]Institute of Materials Research and Engineering, 2 Fusionopolis Way, Singapore 138634, Singapore
[3]Department of Applied Physics, Aalto University School of Science, Espoo FI-02150, Finland
[4]Wyss Institute for Biologically Inspired Engineering, Harvard University, Cambridge, Massachusetts 02138, USA
[5]Kavli Institute for Bionano Science and Technology, Harvard University, Cambridge, Massachusetts 02138, USA

(Received 28 November 2017; published 15 June 2018)

There are currently three main classes of liquid-repellent surfaces: micro- or nanostructured superhydrophobic surfaces, flat surfaces grafted with "liquidlike" polymer brushes, and lubricated surfaces. Despite recent progress, the mechanistic explanation for the differences in droplet behavior on such surfaces is still under debate. Here, we measure the dissipative force acting on a droplet moving on representatives of these surfaces at different velocities $U = 0.01$–$1$ mm/s using a cantilever force sensor with submicronewton accuracy and correlate it to the contact line dynamics observed using optical interferometry at high spatial (micron) and temporal (<0.1 s) resolutions. We find that the dissipative force—due to very different physical mechanisms at the contact line—is independent of velocity on superhydrophobic surfaces but depends nonlinearly on velocity for flat and lubricated surfaces. The techniques and insights presented here will inform future work on liquid-repellent surfaces and enable their rational design.

DOI: 10.1103/PhysRevLett.120.244503

In nature, the ability to repel water is often a matter of life and death. For example, insects must avoid getting trapped by falling raindrops, and plants need to keep their leaves dry for efficient gas exchange through the stomata [1,2]. Similarly, the tendency of water and complex fluids, such as blood and oil, to stick to surfaces poses many challenges to industries, ranging from contamination of biomedical devices to increased hydrodynamic drag in ships [3,4]. Hence, there is a huge interest in developing liquid-repellent materials. To achieve this, there are three main approaches. First, hydrophobic micro- or nanostructures can be designed on the surface to maintain a stable air layer, minimizing contact between the liquid and the solid, i.e., lotus-effect superhydrophobic (SH) surfaces [Fig. 1(a)] [3,5]. Second, a flat surface can be grafted with nanometer-thick "liquidlike" polymer brushes [Fig. 1(b)]; the resulting surface, dubbed a slippery omniphobic covalently attached liquid (SOCAL), is able to repel various liquids, including low-surface-tension alkanes [6–8]. Finally, a suitable lubricant oil can be added to the surface, which can be structured as is the case for slippery liquid-infused porous surfaces [9,10] or flat as is the case of lubricant-infused organogels [11,12] [Fig. 1(c)]; any liquid can then easily be removed, as long as there is a stable intercalated lubricant layer [13–16].

While each of the three surfaces has been studied separately, there have been few attempts to compare their relative liquid-repellent performance. In this Letter, we will elucidate the origin of liquid repellencies for the three surfaces and show how details of the liquid-solid-air three-phase contact line (TPCL) at the droplet's base—or the absence of a TPCL in the case of lubricated surfaces—lead to different droplet dynamics.

Previous work generally reports the static apparent contact angle $\theta_{app}$ and emphasizes the low contact angle hysteresis $\Delta\theta = \theta_{adv} - \theta_{rec} < 10°$, where $\theta_{adv,rec}$ are the

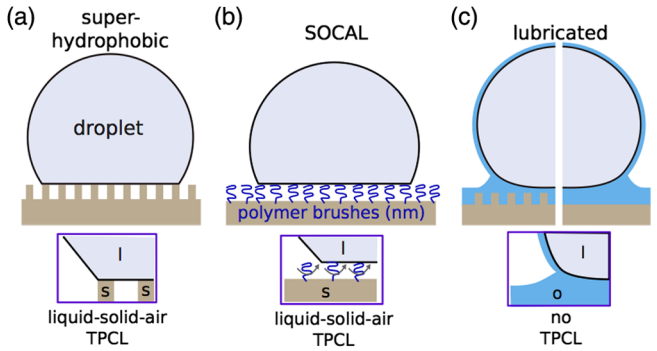


FIG. 1. Schematics of liquid-repellent surfaces. (a) Structured SH surfaces. (b) Flat surfaces grafted with polymer brushes, dubbed SOCAL surfaces. (c) Structured (left) or flat (right) lubricated surfaces. The droplet is shown with a lubricant cloaking layer, which is typical for low-surface-tension lubricants and higher-tension droplets (Supplemental Fig. S1 [17]).

 

TABLE I. Reported contact angle values for a water droplet [17].

| Surface | $\theta_{app}$ | $\Delta\theta$ | $\Delta\cos\theta$ |
|---|---|---|---|
| SOCAL | 90°–110° | 1°–10° | 0.02–0.2 |
| Lotus effect | >150° | 2°–10° | 0.02–0.1 |
| Lubricated | 90°–110° | 1°–5° | 0.02–0.05 |

advancing and receding contact angles, respectively, measured optically from the side (see Table I and Supplemental Tables S1 and S2 [17] for typical values) [27]. The low contact angle hysteresis translates to low dissipative force $F_d$ acting on the droplet, since

$$F_d = 2a\gamma\Delta\cos\theta, \tag{1}$$

where $\Delta\cos\theta = \cos\theta_{rec} - \cos\theta_{adv}$ and $a$ and $\gamma$ are the base radius and the surface tension, respectively (Furmidge's relation) [27,28]. However, for most studies, the exact experimental conditions—in particular, the speed of the contact line $U$—are often not controlled, even though $\Delta\cos\theta$ (and therefore $F_d$) can depend on $U$ [29–33]. Moreover, there are other technical challenges: $\theta$ is difficult to determine accurately when its value is too high $> 170°$ (SH surfaces) [34,35] or when obscured by a wetting ridge (lubricated surfaces) [16].

In this study, to avoid the ambiguity in interpreting contact angle measurements, we measured $F_d$ for a droplet moving at controlled speed $U$ directly using a cantilever force sensor (Fig. 2) [14,36,37]. The droplet was attached to a capillary tube, and the force $F_t(t)$ acting on the droplet was inferred from the tube's deflection $\Delta x(t)$: $F = k\Delta x$, where $k = 5$–$25$ mN/m for tube lengths $L = 6$–$9$ cm. Note that the distortion of the droplet shape due to the tube is minimal (Supplemental Fig. S2 [17]). Details of the custom-built setup can be found in our previous work [14].

Figure 2(a) shows the characteristic force curves for the three surfaces. $F_d$ is taken to be the long-time average, once $F_t$ has reached a steady state. Typically, a larger force $F_{peak}$ is required to jump start the motion, reminiscent of the static and kinetic friction forces between two solid surfaces [37]. For a lotus-effect surface, this $F_{peak} = 6.6$ $\mu$N is sharp and distinct from the force $F_d = 5.0 \pm 0.2$ $\mu$N required to maintain the motion. In contrast, for lubricated and SOCAL surfaces, $F_{peak}$ tends to be broader and less defined. At time $t \approx 50$ s, the droplet motion was stopped: For a lubricated surface with no contact line pinning, the cantilever returned to its original position; in contrast, for SOCAL and lotus-effect surfaces with a TPCL, the droplet was pinned, and $F_t$ did not return to zero but instead reached a finite value $F_{min}$.

As $U$ was varied in the range of 0.01–1 mm/s, we found that $F_d(U)$ acting on a 1 $\mu$l water droplet exhibits different functional forms for the different surfaces, suggesting different mechanistic origins of liquid repellency [Fig. 2(b)]. First, there is a minimum force required to move the droplet on SH and SOCAL surfaces, $F_{min} = 4$ and 5 $\mu$N,

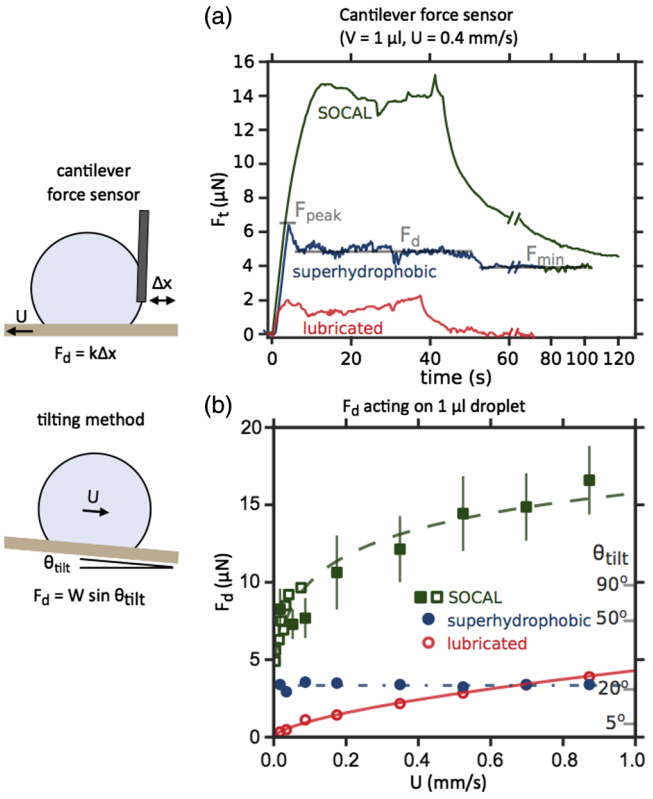


FIG. 2. (a) Characteristic force curves for a water droplet moving on the three surfaces measured using a cantilever force sensor. The motor (to move the substrate) was started at time $t = 0$ s and stopped at $t \approx 50$ s. (b) $F_d$ for 1 $\mu$l water droplets moving at speeds of $U = 0.01$–$1$ mm/s on superhydrophobic (hexagonal array of micropillars with diameter $d = 16$ $\mu$m, pitch $p = 50$ $\mu$m, and height $h_p = 30$ $\mu$m), SOCAL, and lubricated surfaces (filled circles, filled squares, and empty circles, respectively). $U$ of droplets tilted at different $\theta_{tilt} = 25°$–$90°$ on the same SOCAL surface and hence subjected to different $F_d = W\sin\theta_{tilt}$ are shown on the same plot (empty squares). $\Delta F_d < 0.2$ $\mu$N for three repeats, unless otherwise indicated by error bars. See Supplemental Sec. S2 [17] for details on the sample preparation.

respectively; in contrast, for lubricated surfaces, $F_{min} = 0$ [note that $F_{min}$ in Figs. 2(a) and 2(b) are the same]. Second, $F_d$ is independent of $U$ for SH surfaces [dash-dotted line, Fig. 2(b)] but has a nonlinear dependence on $U$ for SOCAL and lubricated surfaces (dashed and solid lines, respectively). To validate the force sensor measurements, velocity data (open squares) of droplets sliding down the same SOCAL surface at different $\theta_{tilt}$ are superimposed on the same plot.

These observations account for the qualitatively different droplet motion on a tilted surface. A 10 $\mu$l water droplet was pinned on SH and SOCAL surfaces, when $\theta_{tilt}$ is below a critical angle $\theta_{crit} \approx 5°$; above $\theta_{crit}$, at $\theta_{tilt} = 15°$, the droplet accelerated at 0.4 m/s$^2$ on the SH surface but moved at constant velocity $U_{const} = 8$ mm/s on the SOCAL surface [Figs. 3(a) and 3(b)]. Eventually, the accelerating droplet on the SH surface will reach a terminal velocity—likely due to air drag—but at a much larger

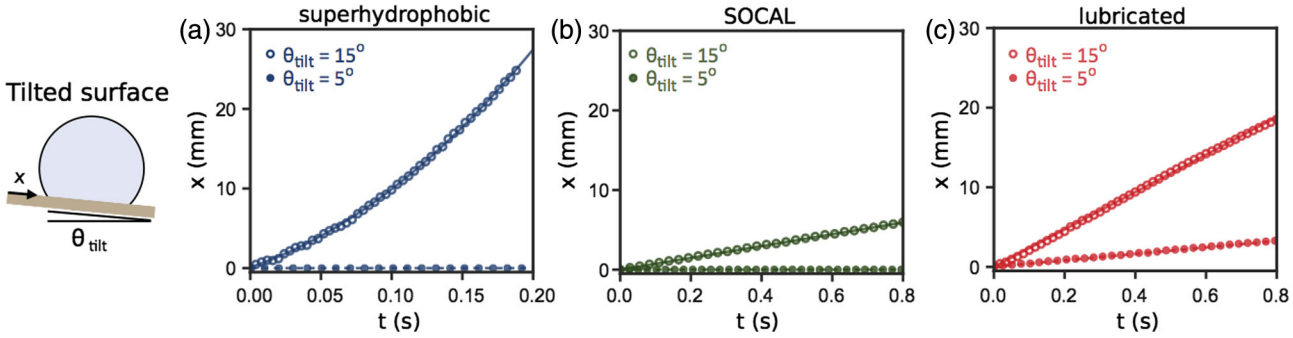


FIG. 3. Droplet motion on surfaces with $\theta_{\text{tilt}} = 5°$ and 15°. Depending on whether a droplet is moving with a constant speed or constant acceleration, the displacement $x$ varies linearly or quadratically with $t$, respectively.

$U_{\text{const}} \sim$ m/s [5]. In contrast, on lubricated surfaces, the droplet was never pinned and moved at increasing $U$ with increasing $\theta_{\text{tilt}}$ [Fig. 3(c)].

To understand the origin and hence the functional form of $F_d$, we analyzed the base of moving droplets using reflection interference contrast microscopy (RICM) (Fig. 4) [38]. We used a similar setup previously to study the lubricant dynamics of lubricated surfaces (Supplemental Sec. S2 [17]) [14]. Using RICM, we were able to confirm the presence of a stable micron-thick air film beneath the droplet on a SH surface and to visualize the details of the contact line with much improved temporal and spatial resolutions compared to other techniques. For example, previous studies using confocal *fluorescence* microscopy usually require a dye to be added to the water droplet—which can affect its wetting properties—-and can achieve only a temporal resolution of $\Delta t$ of several seconds [39]. Environmental scanning electron microscopy (SEM) can achieve submicron spatial resolution but again with a poor $\Delta t$ of about 1 s [40]. Moreover, the high-vacuum and low-temperature conditions of SEM may introduce artifacts and change the viscosity of the liquid(s), which in turn affect droplet behavior [14,41].

Here, using RICM, we visualized the base of a droplet (without dye) moving on a transparent micropillar surfaces with a much improved $\Delta t < 0.1$ s and good spatial details [Fig. 4(a1)]. For example, the distortion of the receding contact line and the accompanying formation of capillary bridges can be observed unambiguously [Figs. 4(a1) and 4(a2)]; we were also able to capture details such as microdroplets that are left behind after the breakup of the capillary bridges, which then evaporate away (Supplemental Figs. S3 and S4 and Supplemental Movie S1 [17]). In contrast to the receding front, the advancing contact line was smooth and continuous [Fig. 4(a3)]; most of the pinning therefore occurs at the receding front, consistent with previous reports [16,42,43].

We can estimate $F_d$ by assuming that the force due to each pillar is $\sim\gamma d$ and the number of pillars in contact at the receding front is $\sim 2a/p$:

$$F_d \sim (2a/p)\gamma d \approx 2a\gamma\phi^{1/2}, \tag{2}$$

where $d$ and $p$ are the pillars' diameter and pitch, respectively, and $\phi$ is the solid surface fraction. We confirmed this scaling law experimentally, with each data point in Fig. 4(a) representing SH surfaces of different

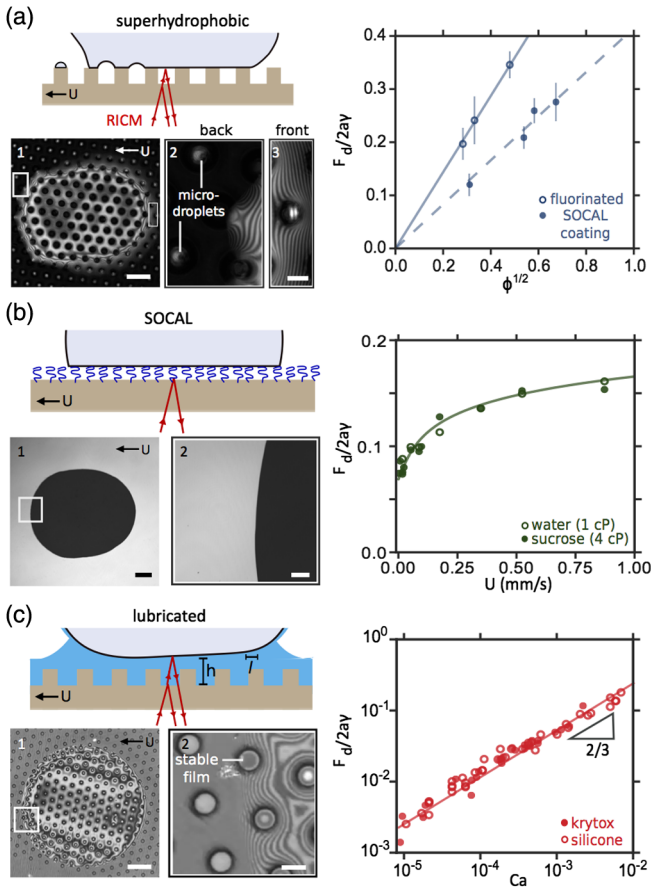


FIG. 4. Reflection interference contrast microscopy is used to visualize (a) the intercalated air film on a SH surface, (b) the contact line on a SOCAL surface, and (c) the intercalated lubricant film on lubricated surfaces. Scale bars are 100 $\mu$m for (a1), (b1), and (c1), 20 $\mu$m for (a2), (a3), and (c2), and 30 $\mu$m for (b2). The dissipative forces $F_d$ are well described by Eqs. (2)–(4). Plots in (a) and (b) are generated from a much larger data set (Supplemental Figs. S5 and S7 [17]). For (b) and (c), the errors $\Delta F_d/2a\gamma$ are $10^{-2}$ and $10^{-3}$, respectively.

$\phi = 0.1$–$0.4$ ($d = 2$–$25$ $\mu$m, $p = 5$–$50$ $\mu$m, and $h_p = 5$–$30$ $\mu$m). The error bar in each data point is the standard deviation observed for water droplets (typically five or more) of volumes $V = 0.5$–$8$ $\mu$l moving at $U = 0.2$–$0.5$ mm/s. The prefactor in Eq. (2) depends on the details of contact line distortion, which in turn depend on the surface functionalization; this explains the two different slopes observed in Fig. 4(a). The model described here, while simple, is able to account for the pinning force on SH surfaces reported here and elsewhere, at least as well as other models previously proposed in the literature (Supplemental Figs. S5 and S6 [17]) [42,44–46].

Using RICM, we were also able to visualize the unique features of the moving contact line on a SOCAL surface at $U = 0.2$ mm/s [Fig. 4(b)]. As was the case with the SH surface, the shape of the contact line was elongated in the direction of motion, but, unlike the SH surface, the receding contact line is smooth without any visibly discrete pinning points [Figs. 4(b1) and 4(b2); cf. Figs. 4(a1) and 4(a2)]. The functional form of $F_d$ for water and 30 wt% aqueous sucrose solution droplets moving at speeds $U = 0.1$–$1$ mm/s is consistent with the molecular-kinetic theory (MKT):

$$F_d = 2a\gamma[\Delta\cos\theta_o + 4K_BT/\gamma\xi^2\mathrm{arcsinh}(U/2K_o\xi)]. \quad (3)$$

In the MKT, the contact line motion is modeled as an absorption-desorption process, with a series of small jumps of size $\xi$ and frequency $K_o$, while $\Delta\cos\theta_o$ is $\Delta\cos\theta$ in the limit of $U \to 0$ (Supplemental Sec. S8 [17]) [29,30]. Viscous dissipation is unimportant, and $F_d$ is indistinguishable between water and 30 wt% sucrose droplets, despite their different viscosities, $\eta = 1$ and 4 cP, respectively [47].

Each data point in Fig. 4(b) is an average of 3–5 droplets with volumes $V = 1$–$5$ $\mu$l, while the line shows the best-fit curve, with $\Delta\cos\theta_o$, $\xi$, and $K_o$ as fitting parameters. The values obtained for $\xi = 3$ nm and $K_o = 7500$ s$^{-1}$ are close to what were reported in the literature for other flat surfaces (Supplemental Table S3 [17]) [48,49]. The value for $\Delta\cos\theta_o = 0.07$, on the other hand, is much lower than typically encountered. For example, a flat glass or silicon surface rendered hydrophobic by fluorosilanization typically has $\theta_{\mathrm{app}} = 110°$ and $\Delta\theta = 15°$–$30°$ or, equivalently, $\Delta\cos\theta_o = 0.3$–$0.5$ [50]. The origin of the low $\Delta\cos\theta_o$ on SOCAL surfaces was hypothesized to originate from the ability of polymer brushes to freely rotate at the moving contact line.

Interestingly, a combination of a SH and SOCAL surfaces, i.e., a micropillar surface coated with the same SOCAL polymer brush [filled circles, Fig. 4(a)], behaves in a qualitatively different way from its flat SOCAL counterpart: $F_d$ no longer depends on $U$ and scales with Eq. (2) rather than Eq. (3). Once again, this confirms that the pinning-depinning process at the microstructured surface is fundamentally different from its chemically analogous flat surface.

TABLE II. Nature of contact angle hysteresis.

| Surface | $F_d/2a\gamma$ or $\Delta\cos\theta$ | Comments |
|---|---|---|
| Superhydrophobic | $\sim\phi^{1/2}$ | No dependence on $U$ |
| SOCAL | $\Delta\cos\theta_o + 4K_BT/\gamma\xi^2$ arcsinh$(U/2K\xi)$ | $\Delta\cos\theta \to \Delta\cos\theta_o$, $U \to 0$ |
| Lubricated | $\sim\mathrm{Ca}^{2/3}$ | $\Delta\cos\theta \to 0$, $U \to 0$ |

For lubricated surfaces, there is no contact line pinning, and hence the droplet base is circular in shape and not elongated [Figs. 4(c1) and 4(c2); cf. Figs. 4(a1) and 4(a2) and Figs. 4(b1) and 4(b2)]. The entrainment of lubricant generates a hydrodynamic lift force, and the droplet levitates over the surface with a film thickness given by the Landau-Levich-Derjaguin law, i.e., $h \sim R\mathrm{Ca}^{2/3}$, where $\mathrm{Ca} = \eta_o U/\gamma_{lo}$ is the capillary number, $\eta_o$ is the viscosity of the lubricant oil, and $\gamma_{lo}$ is the liquid droplet-lubricant-oil interfacial tension [14,51]. $F_d$ is dominated by the viscous dissipation at the rim of the droplet's base of size $l \sim R\mathrm{Ca}^{1/3}$ and is therefore given by

$$F_d \sim (\eta U/h)2al \approx 2a\gamma_{lo}\mathrm{Ca}^{2/3}. \quad (4)$$

This was experimentally verified for droplets of $V = 1$–$5$ $\mu$l moving at $U = 0.01$–$5$ mm/s, with silicone or fluorinated oil of $\eta = 5$–$60$ cP as lubricants [14]. Note that this discussion is true only in the absence of solid-droplet contact; if for some reason the lubricant film becomes unstable, $F_d$ becomes dominated by contact line pinning and is independent of $U$, reminiscent of SH surfaces (Supplemental Fig. S8 [17]).

Comparing Eqs. (2)–(4) with Eq. (1), we can get an expression for the dimensionless force per unit length $F_d/2a\gamma$, which is equivalent to the more conventional (but more ambiguous) $\Delta\cos\theta$, for the different surfaces, as summarized in Table II: $\sim\phi^{1/2}$ for SH surfaces, $\Delta\cos\theta_o + 4K_BT/\gamma\xi^2\mathrm{arcsinh}(U/2K\xi)$ for SOCAL surfaces, and $\sim(\gamma_{lo}/\gamma)\mathrm{Ca}^{2/3} \approx \mathrm{Ca}^{2/3}$ for lubricated surfaces. Recently, there has been some debate on the correct physical interpretation of contact angle hysteresis for lubricated surfaces [14,16,52]. We will address this more fully in a future publication, but, in general, $\Delta\cos\theta \sim \mathrm{Ca}^{2/3}$ corresponds to optical measurements of macroscopic $\cos\theta_{\mathrm{rec}} - \cos\theta_{\mathrm{adv}}$, and Furmidge's relation can still be applied with some modifications (Supplemental Fig. S9 [17]).

In summary, we have clarified the physics behind the three classes of liquid-repellent surfaces, in particular, highlighting their distinct and unique properties, which are not captured by conventional contact angle measurements. We measured the dissipation force $F_d$ with submicronewton accuracy and explicitly showed how the different functional forms of $F_d$ (and, hence, the corresponding contact angle hysteresis) arise from details of the contact line. While we have confined our discussion to

liquid repellency, many of the ideas and techniques outlined here are relevant to various other problems, ranging from ice repellency to the rational design of nonfouling materials.

The work was originated with the support from the Office of Naval Research, U.S. Department of Defense, under MURI Grant No. N00014-12-1-0875 and carried out under Grant No. N00014-17-1-2913. J. V. I. T. was supported by the European Commission through the Seventh Framework Program (FP7) project DynaSLIPS (Project No. 626954). R. L., S. J. V., and A. T. acknowledge the support from the Harvard Materials Research Science and Engineering Center (MRSEC) under Grant No. DMR-1420570.

*daniel@imre.a-star.edu.sg
†jaiz@seas.harvard.edu

[1] W. K. Smith and T. M. McClean, Am. J. Bot. **76**, 465 (1989).
[2] T. Darmanin and F. Guittard, Mater. Today **18**, 273 (2015).
[3] D. Quéré, Annu. Rev. Mater. Res. **38**, 71 (2008).
[4] L. Bocquet and E. Lauga, Nat. Mater. **10**, 334 (2011).
[5] M. Reyssat, D. Richard, C. Clanet, and D. Quéré, Faraday Discuss. **146**, 19 (2010).
[6] J. W. Krumpfer and T. J. McCarthy, Faraday Discuss. **146**, 103 (2010).
[7] D. F. Cheng, C. Urata, M. Yagihashi, and A. Hozumi, Angew. Chem. **51**, 2956 (2012).
[8] L. Wang and T. J. McCarthy, Angew. Chem. **128**, 252 (2016).
[9] T.-S. Wong, S. H. Kang, S. K. Tang, E. J. Smythe, B. D. Hatton, A. Grinthal, and J. Aizenberg, Nature (London) **477**, 443 (2011).
[10] A. Lafuma and D. Quéré, Europhys. Lett. **96**, 56001 (2011).
[11] C. Urata, G. J. Dunderdale, M. W. England, and A. Hozumi, J. Mater. Chem. **3**, 12626 (2015).
[12] J. Cui, D. Daniel, A. Grinthal, K. Lin, and J. Aizenberg, Nat. Mater. **14**, 790 (2015).
[13] J. D. Smith, R. Dhiman, S. Anand, E. Reza-Garduno, R. E. Cohen, G. H. McKinley, and K. K. Varanasi, Soft Matter **9**, 1772 (2013).
[14] D. Daniel, J. V. Timonen, R. Li, S. J. Velling, and J. Aizenberg, Nat. Phys. **13**, 1020 (2017).
[15] A. Keiser, L. Keiser, C. Clanet, and D. Quéré, Soft Matter **13**, 6981 (2017).
[16] F. Schellenberger, J. Xie, N. Encinas, A. Hardy, M. Klapper, P. Papadopoulos, H.-J. Butt, and D. Vollmer, Soft Matter **11**, 7617 (2015).
[17] See Supplemental Material at http://link.aps.org/supplemental/10.1103/PhysRevLett.120.244503 for the details of the experimental setup and theoretical analysis, which includes Refs. [18–26].
[18] B. Pokroy, A. K. Epstein, M. Persson-Gulda, and J. Aizenberg, Adv. Mater. **21**, 463 (2009).
[19] D. S. Bodas, A. Mandale, and S. Gangal, Appl. Surf. Sci. **245**, 202 (2005).
[20] P. Roach, N. J. Shirtcliffe, and M. I. Newton, Soft Matter **4**, 224 (2008).
[21] J. T. Simpson, S. R. Hunter, and T. Aytug, Rep. Prog. Phys. **78**, 086501 (2015).
[22] C. Urata, D. F. Cheng, B. Masheder, and A. Hozumi, RSC Adv. **2**, 9805 (2012).
[23] C. Urata, B. Masheder, D. F. Cheng, and A. Hozumi, Langmuir **29**, 12472 (2013).
[24] P. Kim, T.-S. Wong, J. Alvarenga, M. J. Kreder, W. E. Adorno-Martinez, and J. Aizenberg, ACS Nano **6**, 6569 (2012).
[25] A. F. Stalder, G. Kulik, D. Sage, L. Barbieri, and P. Hoffmann, Colloids Surf., A **286**, 92 (2006).
[26] G. McHale, N. J. Shirtcliffe, and M. I. Newton, Langmuir **20**, 10146 (2004).
[27] P.-G. De Gennes, F. Brochard-Wyart, and D. Quéré, *Capillarity and Wetting Phenomena: Drops, Bubbles, Pearls, Waves* (Springer, New York, 2013).
[28] C. Furmidge, J. Colloid Sci. **17**, 309 (1962).
[29] J. H. Snoeijer and B. Andreotti, Annu. Rev. Fluid Mech. **45**, 269 (2013).
[30] T. D. Blake, J. Colloid Interface Sci. **299**, 1 (2006).
[31] E. Bormashenko, Y. Bormashenko, and G. Oleg, Langmuir **26**, 12479 (2010).
[32] E. Bormashenko, Colloid Polym. Sci. **291**, 339 (2013).
[33] R. Tadmor, P. Bahadur, A. Leh, H. E. Nguessan, R. Jaini, and L. Dang, Phys. Rev. Lett. **103**, 266101 (2009).
[34] S. Srinivasan, G. H. McKinley, and R. E. Cohen, Langmuir **27**, 13582 (2011).
[35] J. T. Korhonen, T. Huhtamki, O. Ikkala, and R. H. Ras, Langmuir **29**, 3858 (2013).
[36] D. Pilat, P. Papadopoulos, D. Schaffel, D. Vollmer, R. Berger, and H.-J. Butt, Langmuir **28**, 16812 (2012).
[37] N. Gao, F. Geyer, D. W. Pilat, S. Wooh, D. Vollmer, H.-J. Butt, and R. Berger, Nat. Phys. **14**, 191 (2018).
[38] J. de Ruiter, F. Mugele, and D. van den Ende, Phys. Fluids **27**, 012104 (2015).
[39] F. Schellenberger, N. Encinas, D. Vollmer, and H.-J. Butt, Phys. Rev. Lett. **116**, 096101 (2016).
[40] K. M. Smyth, A. T. Paxson, H.-M. Kwon, and K. K. Varanasi, Surf. Innovations **1**, 84 (2013).
[41] D. Richard and D. Quéré, Europhys. Lett. **48**, 286 (1999).
[42] M. Reyssat and D. Quéré, J. Phys. Chem. B **113**, 3906 (2009).
[43] L. Gao and T. J. McCarthy, Langmuir **22**, 6234 (2006).
[44] C. W. Extrand, Langmuir **18**, 7991 (2002).
[45] J. Joanny and P.-G. de Gennes, J. Chem. Phys. **81**, 552 (1984).
[46] H.-J. Butt, N. Gao, P. Papadopoulos, W. Steffen, M. Kappl, and R. Berger, Langmuir **33**, 107 (2017).
[47] The force due to viscous dissipation can be estimated by noting that $F_d U = \eta \int_V (\nabla U)^2 dV \approx \eta (U/R)^2 R^3$, i.e., $F_d \sim \eta U R \sim$ nN.
[48] S. R. Ranabothu, C. Karnezis, and L. L. Dai, J. Colloid Interface Sci. **288**, 213 (2005).
[49] R. A. Hayes and J. Ralston, Langmuir **10**, 340 (1994).
[50] D. Quéré, M.-J. Azzopardi, and L. Delattre, Langmuir **14**, 2213 (1998).
[51] L. Landau and V. Levich, Acta Physicochim. URSS **17**, 42 (1942).
[52] C. Semprebon, G. McHale, and H. Kusumaatmaja, Soft Matter **13**, 101 (2017).